Fuel 90 (2011) 3369–3381

Contents lists available at ScienceDirect

Fuel

journal homepage: www.elsevier.com/locate/fuel

Fuel effect on the liquid-phase penetration of an evaporating spray under transient diesel-like conditions

J.V. Pastor [a,*], J.M. García-Oliver [a], J.-G. Nerva [a], B. Giménez [b]

[a] CMT-Motores Térmicos, Universitat Politècnica de València, Camino Vera s/n, 46022 Valencia, Spain
[b] Department of Energy and Fluid Mechanics Engineering, University of Valladolid, Paseo del Cauce s/n, 47011 Valladolid, Spain

ARTICLE INFO

Article history:
Received 17 February 2011
Received in revised form 9 May 2011
Accepted 10 May 2011
Available online 31 May 2011

Keywords:
Diesel engine
Biodiesel
Unsteady spray penetration
Fischer–Tropsch
Liquid length

ABSTRACT

Measurements of the maximum liquid-phase penetration have been performed injecting five different fuels through a single-hole nozzle in an optical engine under a large set of thermodynamic and injection conditions. The focus of this paper is twofold. First, it intends to study fuel physical properties on liquid-phase fuel penetration. The choice made on Fischer–Tropsch diesel (*FTD*) and biodiesel fuels has been highly motivated by their potential to be, at short or middle term, possible substitutes to the conventional diesel fuel. Extensive characterization of fuel physical and chemical properties under ambient conditions are provided and related to the liquid-phase penetration in order to provide an accessible tool to predict liquid spray behavior based on cheap, off-engine measurements. Fischer–Tropsch fuels appeared to be the easiest to vaporize while biodiesel blends were getting always harder to vaporize as the Rapeseed Methyl Ester (*RME*) rate was increased. The second objective of this work is to study the time-response of liquid-phase penetration when subjected to density and temperature variations. Injections of 8 ms at three different pressures have been performed in transient diesel-like conditions with density and temperature time derivatives up to 2000 kg m^{-3} s^{-1} and 20,000 K s^{-1}. In most cases, the spray appeared to closely follow predictions made from empirical models built out of steady-state ambient conditions, leading to the conclusion of an instantaneous adjustment of the spray to its environment, validating: (1) the hypothesis made in 1D spray models; (2) the use of empirical models in unsteady-state environment when obtained under steady-state conditions.

1. Introduction

During the past two decades, research on the effect of fuel properties may not have received fervent interest by the automotive industry, perhaps due to the long-standing establishment of conventional diesel and the lack of viable alternative solutions. Although the studies available on the subject represent precious information for the validation of spray modeling hypothesis [1–4], most of the research effort has been channeled into new combustion concepts using complex injection strategies and high *EGR* levels in order to reduce both NO_X and *PM*. More recently, worldwide environmental agencies have been inciting car constructors to find alternatives to the exhaustible fossil fuel for a better sustainability of energy management [5]. In this ambitious framework, biofuels and synthetic fuels represent an interesting perspective, at least at short and middle term, for their capacity to be directly implanted in the actual car park with no major change of the engine design. Their effect on combustion efficiency and emissions is the result of a complex succession of physical and chemical processes [6]. This study proposes to understand and assess which are the physical mechanisms involved in the introduction of alternative fuels. For this objective, various off-engine measurements have been performed on the five fuels before their injection through a 82 μm-single-hole nozzle, in an optical engine [7] fed with pure nitrogen. The visualization of their respective maximum liquid-phase penetration has been realized under a large set of operating conditions, including a sweep of ambient temperature at constant density, a sweep of ambient density at constant temperature and three different injection pressures have been performed for each fuel. High-speed imaging of the spray shadow left on a highly lit background has been processed to measure the maximum liquid-phase penetration as defined by Dec and Siebers in [8,9]. In the first instance, liquid length results and ambient conditions have been time-averaged as in [10–12] and discussed. In a second instance, unsteadiness of ambient density and ambient temperature during the fuel injection has been used as a way to increase the number of experimental data and consequently the reliability of statistics. For each image and so for each instant of the 8 ms injection event, its corresponding ambient temperature and density were associated. Apart from presenting clear advantages on the statistical point of view [13], these results permitted to conclude on spray reactivity when submitted to variations of ambient density and temperature.

* Corresponding author.
E-mail address: jpastor@mot.upv.es (J.V. Pastor).

0016-2361/$ - see front matter © 2011 Elsevier Ltd. All rights reserved.
doi:10.1016/j.fuel.2011.05.006

Nomenclature

B05/B30	fossil diesel with 5/30% *RME* (in mass)
RME	Rapeseed Methyl Ester
FT (D)	Fischer–Tropsch (Diesel)
LD/HD	Low/High Density condition (at 800 K)
LT/HT	Low/High Temperature condition (at 26 kg m^{-3})
NO	nominal condition
OC	operating conditions

Subscripts

0	refers to initial conditions
f	fuel
amb	refers to the ambient gas surrounding the spray (N_2)
inj	injection
max	maximum
evap	evaporation
back	refers to the spray counter-pressure

Abbreviations

P	pressure
ΔP	Pressure drop = $P_{inj} - P_{back}$
T	temperature
ρ	density
h	enthalpy
K	constant value
X	spray axis
Y	mixture fraction
LL	liquid length
1D	one-dimensional
(A) SOI/E, EOI	(after) start of injection/energizing, end of injection
(A) TDC	(after) top dead center
ASTM	American society for testing and materials
CAD	crank angle degree
CFD	computational fluid dynamics
CMOS	complementary metal-oxide semiconductor
EGR	exhaust gas recirculation
EVO	exhaust valve opening
FID	flame ionization detector
HCCI	homogeneous charge compression ignition
IVC	Intake valve closure
LHV	lower heating value
LRT	likelihood ratio test
NO_X	nitrogen oxides
PM	particulate matter
rpm	revolutions per minute
$R^2_{(spe)}$	(specific) Coefficient of determination
RMSE	root mean square error
$T_{X\%}$	temperature at which X% of the fuel distilled
TTL	transistor–transistor logic

2. Experimental setup

2.1. Fuels

Five different fuels have been selected for their capacity and their potential to be used in a diesel engine with no fundamental redesign of the engine whilst having significant differences in both physical and chemical properties. The first three fuels are widely known in the literature under the generic label "first generation biodiesels". Indeed, they are partially or entirely issued from grain feedstock. Rapeseed Methyl Ester (*RME*) is a fuel resulting from the transesterification reaction between rape oil and methanol. *B*05 and *B*30 are blends of fossil diesel with respectively 5 and 30 mass percentage of the same *RME*.

These three fuels have been previously used by the authors in a multi-hole injector configuration under both reactive and non-reactive environments [11,12]. Finally, the two last fuels are Fischer–Tropsch fuels issued from gas, coal or biomass liquefaction and will be referred as *FT*1 and *FT*2 in the following study. Various measurements of fuel properties have been performed off-engine. Thermodynamic properties, energetic content and equivalent formula have been measured following *ASTM* standards and are summarized in Table 1. Results show that by increasing *RME* rate in biodiesel fuels, both density and viscosity increase as well, whereas *LHV* reduces because of the increasing oxygen content. Both Fischer–Tropsch fuels have a lower density compensated by a higher energetic content, which is an important data under a marketing point of view, since the energetic content of one liter is pretty much the same between all these fuels. *FT*2 is singular by its very low viscosity and its small extra oxygen content. Comparative trends in fluid-mechanics properties were also observed in [14] for a similar selection of fuels. Chemical equivalent formulas have been measured using gas chromatography-FID and are also provided in Table 1. They appear to be close to heptadecane ($C_{17}H_{36}$) and dodecane ($C_{12}H_{26}$) formulas respectively for *FT*1 and *FT*2 while *RME*'s closest pure surrogate could be methyl-oleate ($C_{19}H_{36}O_2$). Distillation curves have been measured under the *ASTM D*86 standard. As mentioned in ASTM D6751, a vacuumed distillation (ASTM D1160) would be more appropriate for *RME* to avoid fuel molecule cracking into lighter fractions at the higher temperature levels expected. However, it still stands biodiesel vaporizing properties compared to the rest of fuels. Besides the classical D86 volume recovery measurement, a weighing scale was measuring the collected mass simultaneously, in order to detect a possible shift between mass and volume recovery percentage. Results are presented in Fig. 1. On one hand, *RME* and *FT*2 appear to have relatively flat distillation curves, which is the witness of their homogeneity and their similitude to their corresponding surrogate. On the other hand, *B*05, *B*30 and *FT*1 have similar trends in evaporation under atmospheric pressure, starting from values close to *FT*2 and ending to values close to *RME*. Consequently, it can be expected that *B*05, *B*30 and *FT*1's lightest fractions are molecules heavier than *FT*2 ($C_{12}H_{25}O_{0.2}$) and that their heaviest fractions are close to *RME*'s molecular weight ($C_{18.95}H_{35.2}O_2$). For *B*05 and *B*30, their *RME* content is expected to correspond to this heavy fraction. No significative differences can be observed on the comparison between mass and volume percentage recovery. This attests that no important variations of density exist among the proper components of each fuel.

While the fuel was getting to the temperature of its first boiling point, an important volume expansion has been observed, measured and translated to density as a function of temperature, considering mass conservation. Results plotted in Fig. 2 show linear trends with high R^2. Coefficients for a linear regression $\rho_f = B + A.T_f$ have been summarized in Table 2. *ASTM D*1298 measurements have been added to the plot as well for illustration, but have not been used in the linear regressions for data consistency. A small offset exists between the *ASTM* measurements and what would be the corresponding measurement by volume at 289 K. Such volume measurements are not as accurate as the *ASTM D*1298 but authors believe that the trend is reliable enough to be used as $\rho_f = \rho_{ASTM\ D1298} + A.(T_f - 289)$. It can be observed how these

Table 1
Fuel relevant properties.

Fuels properties	Unit	ASTM Std.	B05	B30	*RME*	FT1	FT2
Density	(kg m^{-3})	*D1298*	833	849	878	784	773
Kinematic viscosity	(mm^2 s^{-1})	*D445*	2.5	3.1	4.4	3.4	1.3
Lower heating value	(MJ kg^{-1})	*D240*	42.11	41.77	38.24	44.76	44.24
Equivalent chemical formula	–	*D5291*	–	–	$C_{18.95}H_{35.2}O_2$	$C_{17}H_{35.5}$	$C_{12}H_{25}O_{0.2}$
C/H ratio	–	–	–	–	0.538	0.479	0.480
A/F_{st} (20.9% XO_2)	–	–	–	–	12.398	14.748	14.388

coefficients (A) are all slightly inferior to the value for the US diesel ♯2 (0.9) referred by Siebers in [15].

2.2. Hot spray test rig

Tests have operated in a rapid cycling machine which is described in detail in [7] and illustrated in Fig. 3. This facility is based on a modified loop-scavenged single cylinder 2-stroke direct injection diesel engine with three liter displacement and low rated rotational speed (500 rpm). This apparatus makes optical studies on free sprays under inert or reactive diesel-like thermodynamic conditions possible. Intake and exhaust being handled by transfers on the liner, optical access to the high-pressure chamber can be easily achieved through the cylinder head which encloses a cylindrical combustion chamber large enough to avoid spray impingement against engine walls. This chamber has an upper port where a single-hole injector equipped with a 82 μm conical nozzle is mounted, and four lateral orthogonal accesses. One of theses accesses is used by a pressure transducer whereas the three other ones are equipped with oval-shaped quartz windows, 88 mm long, 37 mm large, and 28 mm thick. Although the use of a single-hole injector may produce faster pressure build-up in the nozzle sac-hole, a faster needle lift and a higher pressure at full needle lift [16], it still presented certain benefits compared to the multi-hole one previously used by the authors in the same facility [11]. First, it impeded spray-to-spray interaction (aerodynamic + thermodynamic) and its position relative to the chamber allowed a much larger field for spray development (80 mm) vs. (35 mm). Above all, the mass injected was strongly limited despite the performing of relatively long injections, so that no effect on thermodynamic conditions alteration has been detected on the pressure trace. Indeed, in [11], the use of a multi-hole injector with 130 μm nozzle hole had led the authors to consider the ambient temperature reduction due to fuel vaporization energetic consumption. The window for time-averaging had to be limited in order to consider steady-state environment. More details about the nozzle and injection settings can be found in Fig. 4 and Table 3. For this study, the inert configuration has been set by feeding the engine with pure nitrogen so that any reaction due to air oxygen content was avoided. Consequently, outcomes relative to this work concern exclusively the physical processes associated to fuel injection, atomization, mixing, heat transfer and vaporization. The rig has been operated under a skip fire mode, i.e. one injection event occurs every 20 engine cycles. This strategy is commonly used to minimize windows fouling and to let the system filter the nitrogen and then avoids saturation with vaporized fuel.

2.3. Operating conditions

The test matrix includes five different engine operating conditions which have been selected in order to realize a sweep of three T_{max} at constant ρ_{max} (26 kg m^{-3}) and a sweep of three ρ_{max} at constant T_{max} (800 K) as shown in Fig. 5. The five operating conditions have been labeled *NO*, *LT*, *HT*, *LD*, *HD*, standing respectively for NOminal, Low Temperature, High Temperature, Low Density and High Density ambient setup. The five fuels have been injected at three pressure levels (50, 100 and 150 MPa). The injector was triggered at $-16°ATDC$ and energized during 8 ms ($\approx 24 CAD$ depending on the instantaneous speed close to the TDC of each operating condition). All information relative the injector has been summarized

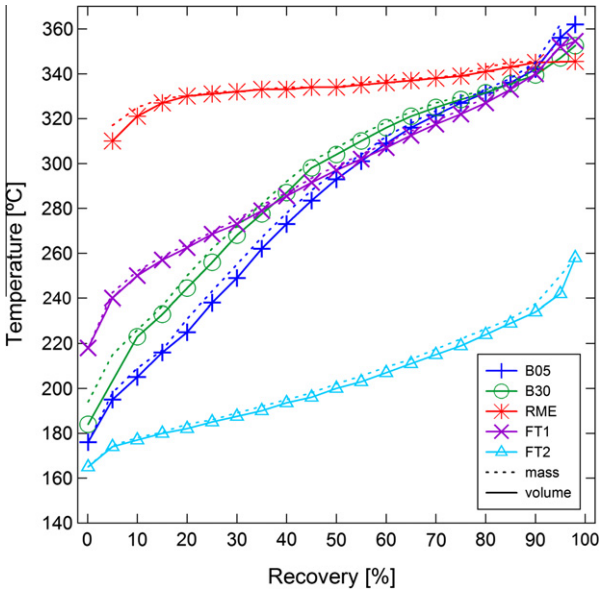

Fig. 1. Distillation curves obtained by *ASTM D86*.

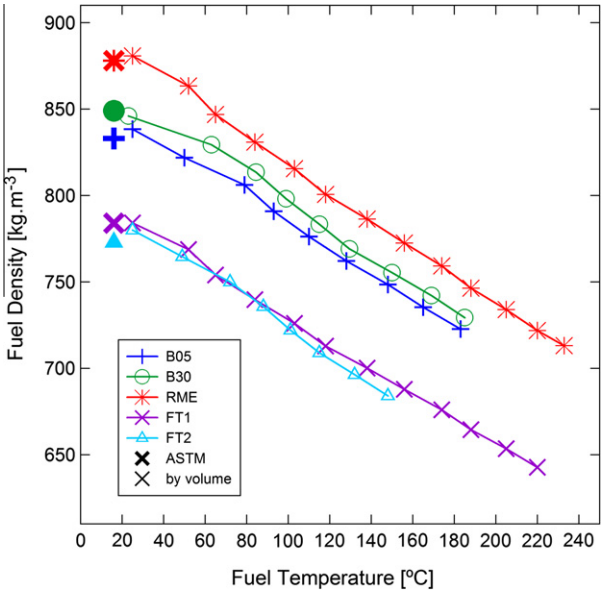

Fig. 2. Temperature effect on fuel density under atmospheric pressure.

Table 2
Linear regression coefficients for fuel density dependency to temperature ($\rho_f = B + A \cdot T_f$).

Coefficients	*B*05	*B*30	*RME*	*FT*1	*FT*2
A	−0.747	−0.759	−0.815	−0.726	−0.804
B	859.5	871.2	900.6	801.8	803.6
R^2 (%)	99.8	99.4	99.8	99.8	99.4

in Table 3. Each test has been repeated 10 times leading to a total number of injections equal to 750 for the whole study (5 *fuels* × 5 *OC* × 3 P_{inj} × 10 *inj.*). To determine the exact intake conditions required by the test plan, an accurate characterization of the engine has been performed over 35 points covering its full range of operating conditions. Thermodynamic conditions have been calculated from the cylinder pressure using a first-law thermodynamic analysis considering blow-by, heat transfer and mechanical stress. First the trapped mass is estimated using intake temperature, intake pressure and volume at IVC (which is rather the exhaust port closure in a 2-stroke engine). Once the trapped mass is known, an apparent temperature can be estimated all along the cycle with the equation of state considering no mass loss. Note that, because of this assumption, even if heat transfer is accounted realistically (this information is in the experimental pressure trace), temperature is underestimated. For this reason, at EVO, this apparent temperature is lower than the one measured in the exhaust pipe. The information of blow-by is contained in this temperature gap. The mass that leaked through blow-by is calculated as the difference between the trapped mass (at IVC) and the mass at EVO at exhaust pressure and temperature. Then, the blow-by mass is distributed all along the cycle *via* a simple algorithm based on Bernoulli's equations for the flow through a nozzle. The equation of state is applied again, with the new "instantaneous mass", geometric volume and experimental pressure, to estimate temperature and density all along the cycle. The mechanical stress applied to the rod can lead to a correction on the instantaneous geometric volume. In this specific engine, no significant deformation was detected. The exact intake conditions for the test plan are interpolated from the 35 points results. A double-check is performed by setting the resulting values to the engine and the reiteration of the same first-law analysis. Intake conditions to carry out the test plan are indicated in Fig. 5. The resulting temperature and densities in the close to TDC region are plotted in Fig. 6.

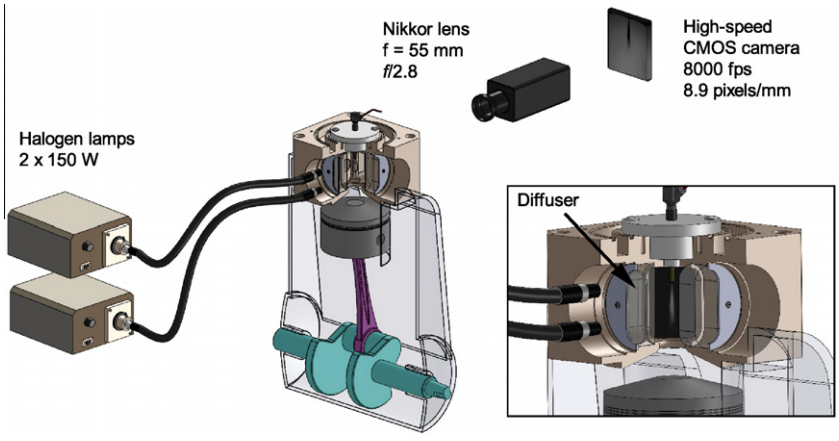

Fig. 3. Hot spray test rig and diffuse back-lightening optical setup.

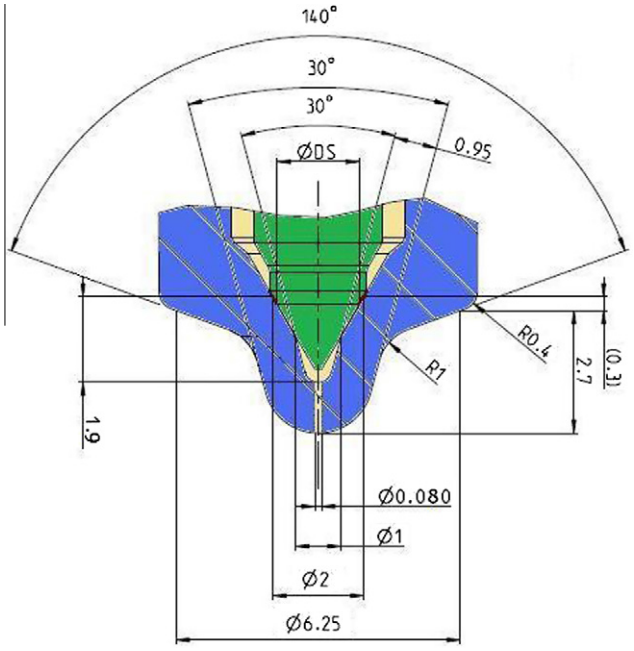

Fig. 4. Cutaway view of the injector tip.

Table 3
Injector characteristics.

Injector	
Injector type	Bosch solenoid
Nozzle type	Mini-sac & Single hole
Nozzle diameter (nominal/measured)	80/82 μm
Nozzle conicity	K 1.5
Injection duration	8 ms
Injection pressures	50, 100, 150 MPa

2.4. Optical setup and image processing

Diffused back-light images have been taken at 8000 fps. Illumination was provided by two 150 W quartz-halogen illuminators (Dolan–Jenner PL800), supplied by 8 mm optic fiber bundles positioned at 60 mm from the diffuser dispensing an illumination of 330 W m^{-2}. The optical setup is represented in Fig. 3. Images of the spray were collected by a high-speed CMOS camera (Photron Fastcam-Ultima APX) equipped with a 55-mm focal length, *f*/2.8 lens. Although exposure time was limited to 25 μs, imaging has been kept to this relatively low frequency in order to keep a reasonable spatial resolution of 8.9 pixels/mm. Camera bit depth of 10 bits allowed a good discretization of digital levels for subsequent image segmentation. The camera was triggered by a *TTL* signal synchronized with the injector electronic start of injection (*SOE*). Each injection event was documented by 100 pictures, accommodating a 12.5 ms acquisition time from the *SOE*.

Images of the spray have been processed with a purpose-made algorithm described in [11,17,18]. Fig. 7 shows two of these processing steps. After a background subtraction (a), a threshold is calculated based on a statistical analysis of each image background [11] and used for image segmentation. Images of diesel sprays can be considered a set of pixel values, each of which belongs to one of two classes according to its digital level: either to the diesel spray itself or to the background. Following this approach, image segmentation can be considered as a classification problem. The discriminant function of the Likelihood Ratio Test (*LRT*) algorithm for the probability-density functions representing both classes is a quadratic form which minimum gives the optimal decision boundary between the background and the diesel spray distributions. Then, only the pixels connected to the spray center of mass are conserved. This step removes the noise left on the segmented image. The distance between the injector tip and the front part of the detected boundary is considered to be the maximum liquid-phase penetration (b).

3. Analysis methodology

As commented in the introduction, data have been processed in two different ways to assess physical processes associated to engine operation and fuel physical properties. After a short theoretical review, the approach of the statistical analysis and its relation to the experiment will be presented.

3.1. Theoretical background

The computational cost of *CFD* motivated investigation for the understanding and the assessment of the phenomena occurring in a diesel spray to simplify the calculation of spray flow-field development. Thus, different 1D-models have been proposed [15,19,20] based on mixing-limited vaporization control, in which hypothesis made are the following: – The spray reaches the complete atomization regime very near the nozzle exit. – Local transfer rates of momentum, mass and energy between liquid droplets and surrounding gas are fast in comparison to the rate of development of the flow field as a whole. This means that an a priori complicated two-phase problem is treated from the point of view of a single-phase flow where a fraction of fuel vaporizes instantaneously once there is enough enthalpy in the surrounding gas to heat it up and vaporize it. The appropriate mixture fraction where this energy balance is achieved is called $Y_{f,evap}$. Consequently, the liquid length, considered as the maximum liquid-phase penetration, could be defined as the position on the spray axis where this specific $Y_{f,evap}$ is reached. Following this hypothesis, a scaling law for liquid length has been derived [21] based on turbulent spray mixing considerations. The axial mass fraction within the quasi-steady part of a diesel spray could be obtained from:

$$Y_f = K \cdot d_0 \sqrt{\frac{\rho_f}{\rho_{amb}}} \cdot \frac{1}{X} \tag{1}$$

where K states for a spray constant, d_0 is nozzle diameter, ρ_f and ρ_{amb} fuel and ambient density and X is spray axial coordinate. Thus, liquid length is defined by:

$$LL = K \cdot \left[d_0 \sqrt{\frac{\rho_f}{\rho_{amb}}} \right] \cdot \frac{1}{Y_{f,evap}} \tag{2}$$

In Eq. (2), the term in brackets is widely known in the literature as the equivalent diameter and is related to spray mixing scales (i.e. momentum) while the last one, as stated before, is an energy term which takes into account vaporization processes. This last term could be written as in Eq. (3), where T_{amb} is ambient gas temperature, $T_{f,0}$ is the initial fuel temperature and T_{evap} is the saturation temperature when the fuel is fully vaporized.

$$\frac{1}{Y_{f,evap}} = 1 + \frac{\Delta h_f(T_{evap}, T_{f,0})}{\Delta h_{amb}(T_{amb}, T_{evap})} \tag{3}$$

This parameter shows a complex dependence on both fuel properties and ambient thermodynamic conditions [15,21] such as temperature, fuel specific and latent heat, and fuel initial temperature.

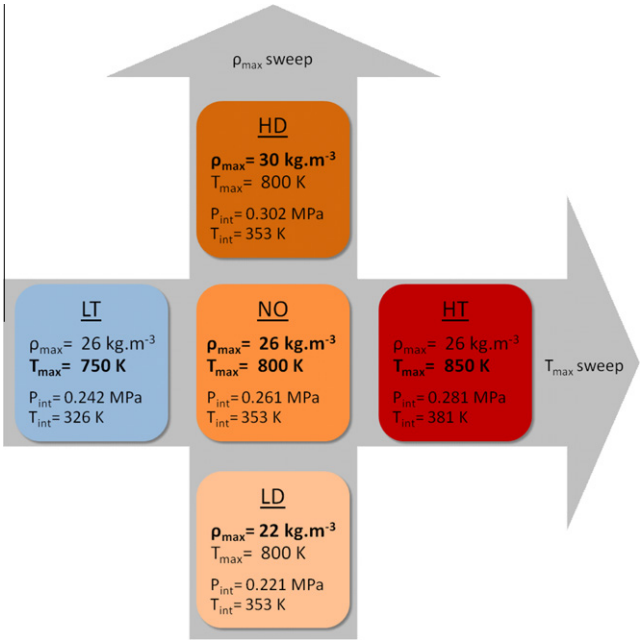

Fig. 5. Schematic representation of the engine operating conditions.

3.2. Statistical analysis

These theoretical considerations have been applied in a statistical study in order to analyse experimental results and check hypotheses reliability. This study aims at relating liquid length with operating conditions and fuel characteristics. The following model for the dependence of liquid length has been proposed:

$$LL \propto D_{noz}^{a} \cdot T_{amb}^{b} \cdot P_{inj}^{c} \cdot \rho_{amb}^{d} \cdot \rho_{f}^{e} \cdot v_{f}^{f} \cdot T_{10\%}^{g} \cdot T_{50\%}^{h} \cdot T_{95\%}^{i} \quad (4)$$

The classical correlations for liquid length in diesel sprays have been completed with some factors particular to the fuel so that fuel

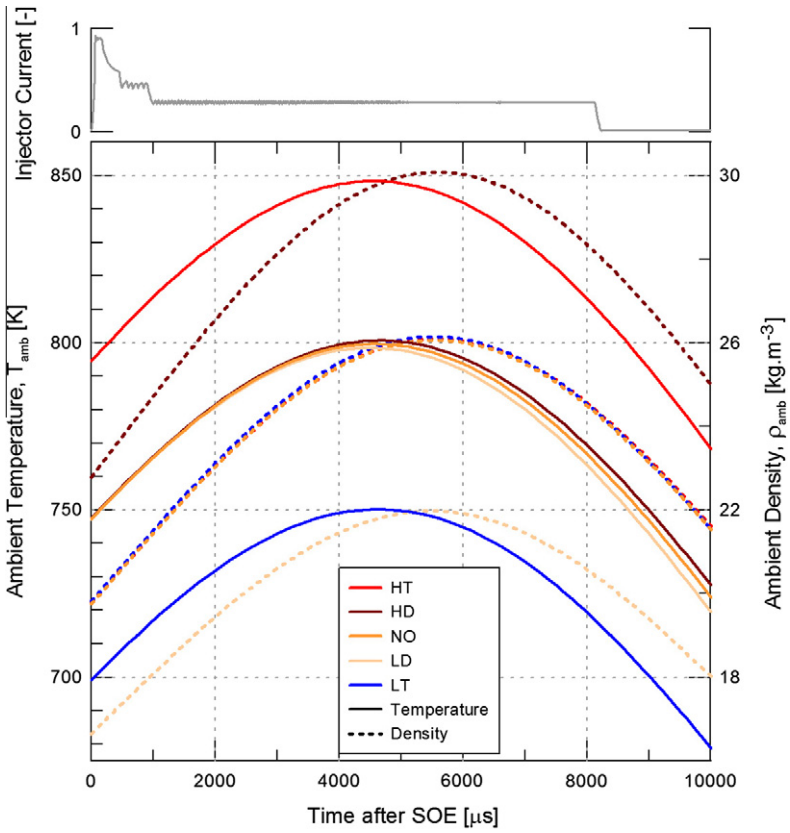

Fig. 6. Results of in-cylinder first-law thermodynamic analysis for temperature and density calculation in the *TDC* region. Eight milliseconds injection duration is represented by the injector current.

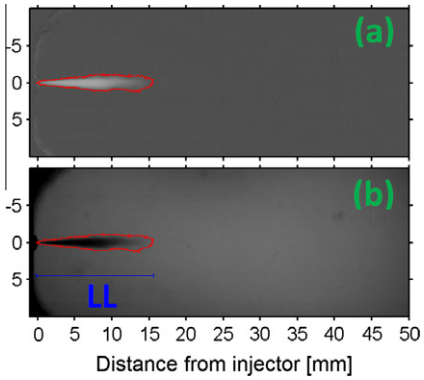

Fig. 7. Intermediate processing images from FT2 at BT and P_{inj} = 100 MPa. (a) Resulting image from original image subtraction to the background. (b) Overlay of the boundary resulting from the complete processing to the original image.

fluid-mechanical and vaporizing properties are accounted. Coefficients b, c, d from Eq. (4) have been previously evaluated independently for each fuel under both steady and unsteady conditions. Nozzle diameter effect has not been studied so D^{a}_{noz} will be consequently part of the constant factor. An injection pressure exponent has been retained, despite the fact that injection velocity (and thus injection pressure) has theoretically no influence on liquid length.

3.3. Quasi-steady-state conditions approach

The assumption of steady-state conditions has already been made by the authors in previous studies [11,12] and so liquid length was considered to be constant around engine *TDC* to resolve exponents from Eq. (4). A window for time-averaging is selected on the stabilized liquid-length region. The engine first-law thermodynamic analysis showed that the engine reaches T_{max} between −2.8 and −3.1°*ATDC* (4500 and 4625 μs *ASOE*) and ρ_{max} between −0.1 and −0.5°*ATDC* (5500 and 5625 μs *ASOE*), depending on the engine operating conditions. Therefore, time-averaging window has been limited between 3500 and 6500 μs *ASOE*. Fig. 8 shows a plot of the ensemble average and its standard deviation. The section used for time-averaging has been highlighted and the result plotted in dashed line. Images from one of the 10 corresponding sequences have been added for illustration. Only one image out of two has been displayed to simplify the figure.

Only the most relevant results of this analysis have been plotted in the Section 4 but the whole set of numerical results is provided in an appendix table.

3.4. In-cylinder unsteady conditions approach

In order to check if both empirical models based on results obtained under steady-state conditions and spray models based on a succession of quasi-steady evaporating states [15,19] are extendable to real engine conditions, most of the image sequence has been exploited by attributing to each image of the spray its corresponding couple of T_{amb} and ρ_{amb} and resolve Eq. (4) in terms of time-resolved values. As commented in the experimental apparatus description, the spray is exposed to important pressure variations. On Fig. 5, it can be observed how T_{amb} fluctuates over more than 50 K and so does ρ_{amb} by up to 7 kg m^{-3} during the injection event (≈24*CAD*). This is due to the relative long injection timing (8 ms) compared to engine speed (500 rpm). Fig. 8 shows how the in-cylinder pressure leaves its mark on the ensemble-averaged liquid length. Temperature and density time-derivatives have been plotted in Fig. 9. It is worthy to note that despite the temporal vari-

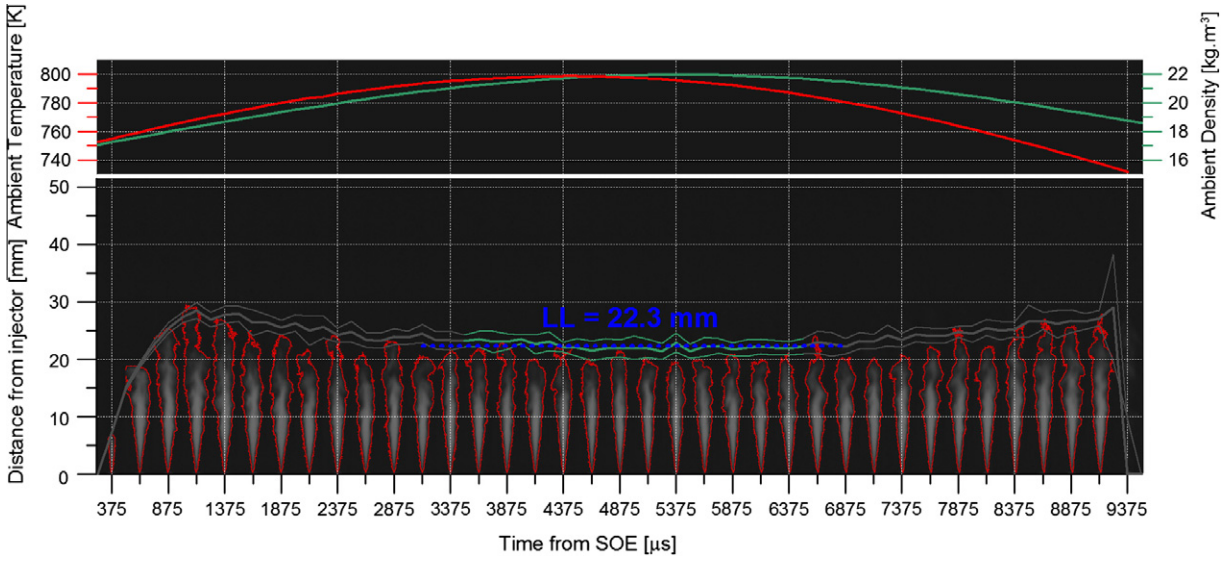

Fig. 8. Representation of the cycle-to-cycle averaging and standard deviation (from 10 repetitions) for *FT*1, Low Density (22 kg m^{-3}; 800 K) at 50 MPa injection pressure. Images (1 out of 2) from one cycle have been added for illustration. The time-averaging window (3500–6500 μs *ASOE*) is represented in green and the time-averaged value dashed blue line. $\rho_{amb}(t)$ and $T_{amb}(t)$ are represented in the upper part of the figure. (For interpretation of the references to color in this figure legend, the reader is referred to the web version of this article.)

ations seem to be small, they are of the order of expected variations in a heavy-duty engine at 1200 rpm in the injection region for *HCCI* combustion mode and in the close-to-*TDC* region for a conventional combustion mode. For this analysis, the time window used for analysis had also to be restricted to avoid the consideration of *SOI* and *EOI* penetration transients. As an example, the case exposed in Fig. 8, has been restricted between 1375 and 8875 μs *ASOE*. The liquid length results have been reprocessed using the same statistical method described above in order to assess the effect of in-cylinder conditions. From a statistical point of view, such kind of study is very interesting since it multiplies the combinations of T_{amb} and ρ_{amb}. Moreover, blow-by, heat transfer and mechanical stresses induce a delay between both traces and reduce collinearity between both variables.

4. Results and discussion

4.1. Quasi-steady-state conditions

The liquid length at different injection pressures has been plotted for the five studied fuels in Fig. 10. Significant differences can be observed from one fuel to another given the reduction by more than a factor of two between *RME* and *FT2* liquid lengths. Both of these fuels constructed the upper and lower boundaries of the tested fuels, respectively. Fig. 10 shows similar trends regarding two fuels encasing the others by upper and lower boundaries as in Fig. 1, which illustrates the high influence of fuel volatility. Such result was then expected since the association between liquid length and distillation curves is already widely assumed in the literature [3,9,4]. Recent works available on the subject still use this measurement to explain both the shorter *FTD* liquid length [22] and the higher biodiesel liquid length [23,24] respective to the conventional diesel. A slight decrease of the liquid length can be observed among all the fuels when injection pressure is increased. However, this effect is small enough to consider this result in agreement with the "mixing-controlled" assumption. Although only the *NO*-condition is represented, the same trends have been observed for the four other operating points. Since it has just been confirmed that injection pressure had no considerable effect on liquid-phase penetration, the effects of ambient temperature and ambient density have been represented only for the 150 MPa injection pressure case in Figs. 11 and 12. Again, the fuel hierarchy is conserved and is quite consistent with the distillation curves at ambient pressure. For all fuels, an increase on both ambient parameters leads to a reduction of the liquid length. Likewise, the effect of T_{amb} appears to be extremely significant. Indeed, a 13% increase of ambient temperature affects up to a 43% decrease on the liquid length, while a 36% increase of ambient density only decreases the liquid length by up to a 25%. It must be highlighted that the 100 K variation applied in this study is far from covering the whole range of temperatures encountered in a diesel engine. Consequently, in early and late injection strategies, where the ambient temperature is expected to be even lower, the resulting liquid length, enhanced by the lower density as well, could lead to an important liner-impingement if care is not taken during the hardware design. The purpose of the following section is precisely to assess the weight of these parameters by means of the previously described statistical analysis.

4.2. Statistical regression for engine-depending physical processes assessment

In a first instance, the statistical analysis has been applied to each fuel independently, introducing only the parameters which

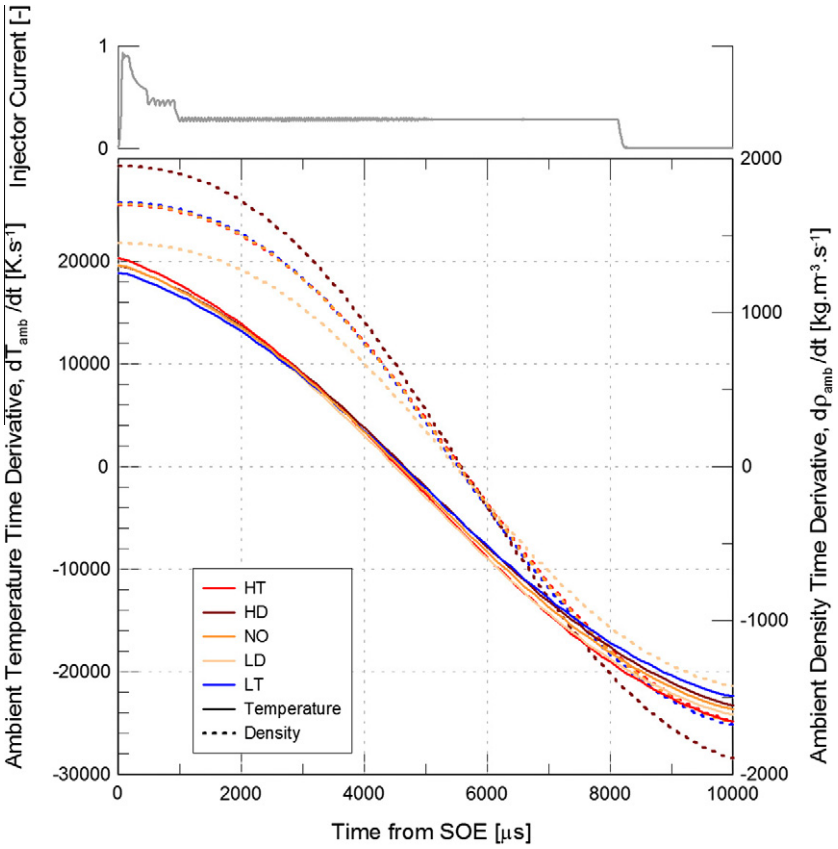

Fig. 9. Temperature and density time-derivatives during the injection event.

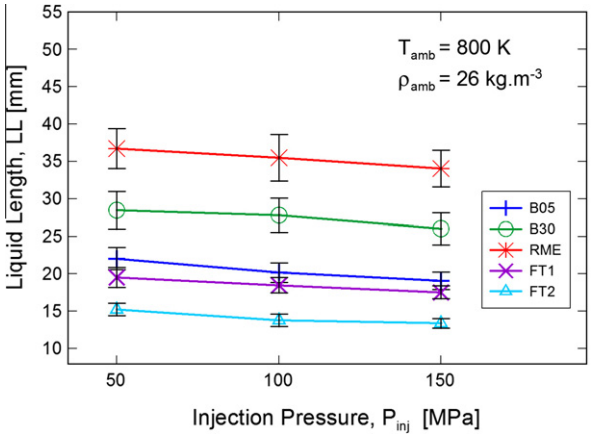

Fig. 10. Injection pressure effect on liquid length for the five studied fuels at NO ambient conditions.

change with the operating settings of the engine. In this way it is proposed to check if all fuels have the same sensitivity to engine parameters. T_{amb}, ρ_{amb} and P_{inj} effect have been assessed and are presented in Table 4. Both temperature high impact and injection pressure irrelevance are confirmed while ambient density effect seems to be a bit higher than proposed by the scaling law. Moreover, from one fuel to the other, slight differences are appreciated, indicating a difference on fuel response to engine thermodynamic settings. Indeed, *RME* seems to be more gently affected by in-cylinder conditions, way above the rest. If results from steady and unsteady-state are now considered for comparison, it can be observed that, exception made for *RME*, the resulting exponents are remarkably close. It may be necessary to remind here that the "steady-state" exponents have been obtained using a set of averaged data coming from a sweep of three ambient density values at constant ambient temperature and from a sweep of three ambient temperature values at constant ambient density, both fueled at three injection pressures levels (15 values/fuel), while "unsteady-state" considers ambient density and temperature values during the entire injection event for both sweeps (≈900 values/fuel). This parallelism in the results indicates that a spray under unsteady conditions behaves as a succession of sprays obtained under steady-state conditions, meaning that there is no delay in the spray adjustment to its environment under the range of pressure derivatives studied. This result is in agreement with recent studies [25] and validates the use of theoretical 1D spray models [15,19,20] in unsteady conditions as well as empirical models based on liquid length measurements obtained in a steady-state environment. Such conclusions are supported by the high correlations reliability that has been evaluated through the R-squared parameter which is, apart for *RME*, consistent between steady and unsteady-state conditions.

The differences observed on exponents for *RME* as well as the decay observed on R^2 show that this fuel may not follow the same conclusions depicted above and that the characteristic time of vaporization for a droplet of such a dense, viscous and low volatility fuel may be significant compared to the spray flow field development. In [23], Fisher et al. performed a similar analysis as in [25] but using two biodiesel fuels. They also observed that biodiesel liquid length is not directly related to instantaneous in-cylinder temperature and density, and suggest that biodiesel may be subject to the thermodynamic history. An attempt has been made to quantify the biodiesel time-response. However the quality of the result showed to be highly affected by our relatively low camera frequency. Yet, no clear trends were found when this delay was correlated either with engine parameters or with the proper liquid length. Thus, both data and correlations were not robust enough to be presented in this manuscript and more investigation on the subject will be needed. Finally, liquid length results from all the fuels have been introduced to the statistical analysis simultaneously. As expected, if no dramatic effect can be observed on exponents' values, the very low R^2 shows that physical parameters issued from the engine setup are not sufficient to predict liquid length and that it is necessary to introduce fuel physical properties to achieve a better prediction.

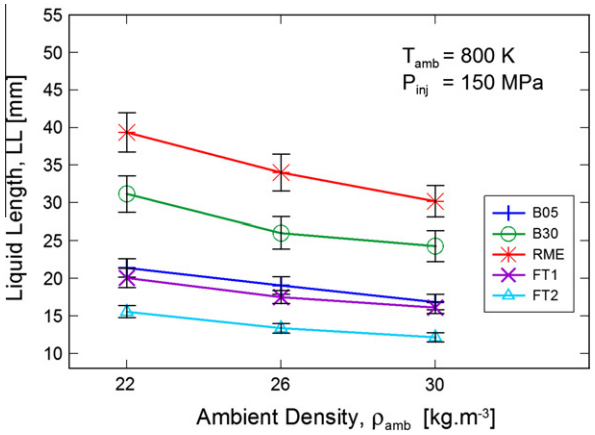

Fig. 11. Ambient density effect on liquid length for the five studied fuels at 150 MPa injection pressure.

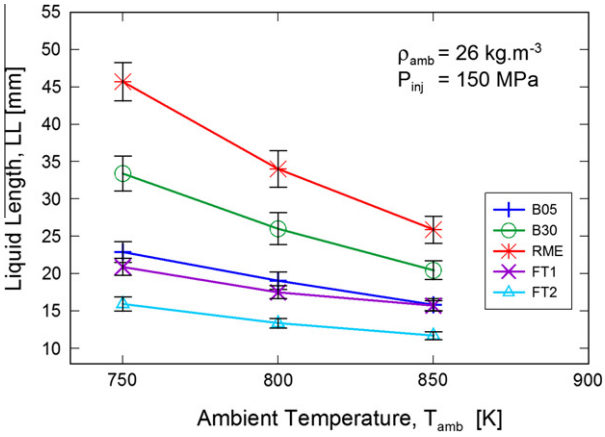

Fig. 12. Ambient temperature effect on liquid length for the five studied fuels at 150 MPa injection pressure.

Table 4
Results from the statistical analysis for assessment of engine physical conditions under both steady and unsteady conditions. Statistically insignificant exponents (p-value > 0.05) appear in italic.

Parameter		Cte	d_0	T_{amb}	P_{inj}	ρ_{amb}	–	–
Exponents		–	a	b	c	d	R^2	RMSE
Theoretical		–	1	−1.58	0	−0.5	–	–
B05	*Steady-State*	3.0324E+11	–	−3.11	−0.10	−0.68	99.0	0.28
B30		3.7266E+10	–	−2.80	*−0.02*	−0.70	92.6	0.91
RME		3.2664E+15	–	−4.39	*−0.04*	−0.82	99.0	0.59
FT1		5.3889E+09	–	−2.55	−0.09	−0.63	99.3	0.19
FT2		1.1733E+10	–	−2.68	−0.10	−0.67	97.9	0.26
All fuels		1.2095E+11	–	−2.98	*−0.06*	*−0.69*	15.3	6.95
B05	*Unsteady-State*	3.0139E+11	-	−3.12	−0.10	−0.66	96.5	0.60
B30		3.9238E+10	–	−2.81	−0.02	−0.69	89.4	1.23
RME		7.9248E+12	–	−3.55	−0.01	−0.75	88.9	2.02
FT1		4.4816E+09	–	−2.54	−0.09	−0.60	97.4	0.43
FT2		3.1336E+09	–	−2.53	−0.09	−0.58	95.5	0.44
All fuels		9.9393E+08	–	−2.42	−0.05	−0.39	11.3	6.82

4.3. Statistical regression for fuel physics assessment

The same statistical tool has been applied, introducing data from the measured fuel physical properties exposed in the upper corresponding section. They have been separated in two parts: fluid-mechanics and evaporative properties. Fluid-mechanics properties are represented by density and viscosity while evaporative properties, in absence of specific and latent heat, are represented by $T_{10\%}$, $T_{50\%}$ and $T_{95\%}$ from distillation curves. Indeed, the purpose of the resulting correlations is to provide a tool that predicts liquid length out of cheap, off-engine measurements. A set of selected correlations are presented in Table 5 by using only some of the terms in Eq. (4). In order to compare correlations with a different number of parameters, reliability has been calculated using specific R-squared (R^2_{spe}). As in the previous section, no significative differences have been observed between steady and unsteady-state considerations and therefore, only unsteady-state conditions are reported in Table 5. First, physical properties issued from the engine operation and fuel physical properties have been compared in correlations (1) and (2). It appears that fuel properties are more important than physical in the prediction of liquid length. However negative coefficients for $T_{10\%}$ and $T_{95\%}$ are not physically reasonable. It is important then to identify, among the five physical parameters, which are controlling the process. In correlations (3) and (4) (5) (6) (7), each fuel parameter has been associated to one physical parameters issue from the engine. Fuel density seems to be the best parameter for liquid length prediction, while no significant differences can be observed separating the three distillation curve temperatures. However the low R^2 for $T_{95\%}$ is unacceptable. In correlations (8) and (9), the fuel fluid mechanics properties and fuel evaporative properties are respectively associated to engine physical properties. The result is that they are both good groups of variables for empirical modeling, although, again, the negative exponents for $T_{10\%}$ and $T_{95\%}$ are a physical non-sense. Finally, correlation (10) shows the association of both fluid-mechanics and evaporative properties using the most essential and reliable parameters. This correlation is consequently considered by the authors as the most significant among the 10 ones shown in the table. Correlation (11) has been added to show the maximum reliability these parameters are capable of, for comparison with upper correlations.

5. Summary and conclusions

Measurements of the maximum liquid-phase penetration have been performed using five fuels with an interesting potential for diesel substitution, in an optical engine under a large set of thermodynamic and injection conditions. These measurements have been related to fuel properties measurements performed off-engine and to pressure variations similar to those found in a heavy-duty diesel engine, in order to assess the physical processes controlling the vaporization of a spray under such conditions. Relevant conclusions are the following:

Table 5
Results from the statistical analysis for assessment of engine physical conditions and fuel physical properties under unsteady-state conditions.

Parameter			Cte	d_0	T_{amb}	P_{inj}	ρ_{amb}	ρ_f	v_f	$T_{10\%}$	$T_{50\%}$	$T_{95\%}$	–	–
Exponents		♯	–	a	b	c	d	e	f	g	h	i	R^2_{spe}	RMSE
Theoretical			–	1	−1.58	0	−0.5	0.5	–	–	–	–	–	–
All fuels	*Unsteady-State*	(1)	9.9393E+08	–	−2.42	−0.05	−0.39	–	–	–	–	–	11.3	6.82
		(2)	1.0000E+00	–	–	–	–	0.71	0.22	−1.14	5.41	−4.53	78.2	3.45
		(3)	8.2699E−08	–	−2.78	−0.06	−0.61	5.99	–	–	–	–	88.7	2.57
		(4)	6.8209E+09	–	−2.72	−0.06	−0.55	–	0.62	–	–	–	79.5	3.15
		(5)	9.4517E+06	–	−2.68	−0.06	−0.54	–	–	1.27	–	–	75.1	3.80
		(6)	3.2668E+06	–	−2.66	−0.06	−0.54	–	–	–	1.39	–	69.0	4.10
		(7)	1.5327E+06	–	−2.51	−0.06	−0.47	–	–	–	–	1.27	45.4	5.01
		(8)	2.2874E−03	–	−2.74	−0.06	−0.61	4.39	0.26	–	–	–	94.6	1.62
		(9)	1.8131E+10	–	−2.85	−0.07	−0.63	–	–	−1.23	6.94	−5.45	97.9	0.97
		(10)	**6.1213E-05**	**–**	**−2.63**	**−0.06**	**−0.60**	**4.39**	**–**	**–**	**0.54**	**–**	**94.4**	**1.57**
		(11)	1.0000E+00	–	−2.85	−0.07	−0.63	6.61	1.70	−0.90	−2.89	−0.06	98.1	0. 93

1. A database of fuel properties and time-averaged liquid-length results are provided for comparison with modeling results (Cf. Appendix A).
2. Under all tested conditions, Fischer–Tropsch fuels showed to have a shorter liquid length than biodiesel fuels, for which the liquid length was increased as the *RME* percentage was increased as well. The fuel hierarchy for liquid length was the following: *FT*2 < *FT*1 < *B*05 < *B*30 < *RME*. This trend was maintained for all engine settings.
3. The qualitative effects of T_{amb}, ρ_{amb} and P_{inj} already available in the literature for diesel fuel have been confirmed and could be extended to biodiesel and Fischer–Tropsch fuels.
4. A new method, based on time consideration, has been proposed for the processing liquid length high speed imaging. It permitted to multiply the number of samples for a more robust statistical analisis.
5. For 4 out of the 5 tested fuels, the comparison between two statistical approaches showed that the spray liquid-phase adjust instantaneously to the in-cylinder conditions. Such results confirms the hypothesis made by 1D spray models and allows the use of empirical models obtained under steady-state environment in unsteady conditions (with time-derivatives up to 20,000 K s^{-1} and 2000 kg m^{-3} s^{-1}).
6. Fuel physical properties have been assessed against the physical properties resulting from engine operating conditions and translated into correlations for empirical modeling.
7. A correlation based on low cost off-engine measurements is proposed taking into account engine parameters, fuel fluid-mecanics properties and evaporation properties: $LL \propto T_{amb}^{-2.63}.P_{inj}^{-0.06}.\rho_{amb}^{-0.60}.\rho_f^{4.39}.T_{50\%}^{0.54}$

Acknowledgments

The authors wish to acknowledge the Spanish Ministry of Education and Science for the financial support through the OPTICOMB project (TRA2007-67961-C03-01) and Jean-Guillaume Nerva's Grant (BES-2008-004420). The authors would also like to thank Daniel Lerida for the management of the facility and his assistance in data acquisition.

Appendix A

Fuel	T_{amb} (K)	ρ_{amb} (kg m^{-3})	P_{inj} (MPa)	ΔP (MPa)	ρ_f (kg m^{-3})	v_f (mm^2 s^{-1})	$T_{10\%}$ (K)	$T_{50\%}$ (K)	$T_{95\%}$ (K)	LL (mm)
B05	798.0	29.7	50	43.2	833	2.50	205	293	356	19.34
	798.0	29.7	100	93.2	833	2.50	205	293	356	18.42
	798.0	29.7	150	143.2	833	2.50	205	293	356	16.87
	845.2	25.8	50	43.7	833	2.50	205	293	356	17.83
	845.2	25.8	100	93.7	833	2.50	205	293	356	16.55
	845.2	25.8	150	143.7	833	2.50	205	293	356	15.84
	795.4	21.7	50	45.1	833	2.50	205	293	356	24.01
	795.4	21.7	100	95.1	833	2.50	205	293	356	22.68
	795.4	21.7	150	145.1	833	2.50	205	293	356	21.42
	747.5	25.9	50	44.5	833	2.50	205	293	356	25.64
	747.5	25.9	100	94.5	833	2.50	205	293	356	24.87
	747.5	25.9	150	144.5	833	2.50	205	293	356	22.90
	796.8	25.8	50	44.1	833	2.50	205	293	356	22.05
	796.8	25.8	100	94.1	833	2.50	205	293	356	20.17
	796.8	25.8	150	144.1	833	2.50	205	293	356	19.07
B30	798.0	29.7	50	43.2	849	3.10	223	304	347	24.53
	798.0	29.7	100	93.2	849	3.10	223	304	347	26.15
	798.0	29.7	150	143.2	849	3.10	223	304	347	24.28
	845.2	25.8	50	43.7	849	3.10	223	304	347	24.16
	845.2	25.8	100	93.7	849	3.10	223	304	347	23.07

(*continued on next page*)

Appendix A (*continued*)

Fuel	T_{amb} (K)	ρ_{amb} (kg m^{-3})	P_{inj} (MPa)	ΔP (MPa)	ρ_f (kg m^{-3})	ν_f (mm^2 s^{-1})	$T_{10\%}$ (K)	$T_{50\%}$ (K)	$T_{95\%}$ (K)	LL (mm)
	845.2	25.8	150	143.7	849	3.10	223	304	347	20.48
	795.4	21.7	50	45.1	849	3.10	223	304	347	30.58
	795.4	21.7	100	95.1	849	3.10	223	304	347	31.86
	795.4	21.7	150	145.1	849	3.10	223	304	347	31.17
	747.5	25.9	50	44.5	849	3.10	223	304	347	30.93
	747.5	25.9	100	94.5	849	3.10	223	304	347	32.08
	747.5	25.9	150	144.5	849	3.10	223	304	347	33.41
	796.8	25.8	50	44.1	849	3.10	223	304	347	28.49
	796.8	25.8	100	94.1	849	3.10	223	304	347	27.80
	796.8	25.8	150	144.1	849	3.10	223	304	347	26.03
RME	798.0	29.7	50	43.2	878	4.41	321	334	345	31.67
	798.0	29.7	100	93.2	878	4.41	321	334	345	29.57
	798.0	29.7	150	143.2	878	4.41	321	334	345	30.20
	845.2	25.8	50	43.7	878	4.41	321	334	345	27.80
	845.2	25.8	100	93.7	878	4.41	321	334	345	27.57
	845.2	25.8	150	143.7	878	4.41	321	334	345	25.88
	795.4	21.7	50	45.1	878	4.41	321	334	345	39.14
	795.4	21.7	100	95.1	878	4.41	321	334	345	40.63
	795.4	21.7	150	145.1	878	4.41	321	334	345	39.36
	747.5	25.9	50	44.5	878	4.41	321	334	345	38.71
	747.5	25.9	100	94.5	878	4.41	321	334	345	45.85
	747.5	25.9	150	144.5	878	4.41	321	334	345	45.69
	796.8	25.8	50	44.1	878	4.41	321	334	345	36.73
	796.8	25.8	100	94.1	878	4.41	321	334	345	35.50
	796.8	25.8	150	144.1	878	4.41	321	334	345	34.03
FT1	798.0	29.7	50	43.2	784	3.44	250	297	352	18.26
	798.0	29.7	100	93.2	784	3.44	250	297	352	17.33
	798.0	29.7	150	143.2	784	3.44	250	297	352	16.12
	845.2	25.8	50	43.7	784	3.44	250	297	352	17.07
	845.2	25.8	100	93.7	784	3.44	250	297	352	15.90
	845.2	25.8	150	143.7	784	3.44	250	297	352	15.72
	795.4	21.7	50	45.1	784	3.44	250	297	352	22.31
	795.4	21.7	100	95.1	784	3.44	250	297	352	20.79
	795.4	21.7	150	145.1	784	3.44	250	297	352	20.08
	747.5	25.9	50	44.5	784	3.44	250	297	352	23.28
	747.5	25.9	100	94.5	784	3.44	250	297	352	22.22
	747.5	25.9	150	144.5	784	3.44	250	297	352	20.92
	796.8	25.8	50	44.1	784	3.44	250	297	352	19.53
	796.8	25.8	100	94.1	784	3.44	250	297	352	18.48
	796.8	25.8	150	144.1	784	3.44	250	297	352	17.54
FT2	798.0	29.7	50	43.2	773	1.29	177	200	242	13.53
	798.0	29.7	100	93.2	773	1.29	177	200	242	13.09
	798.0	29.7	150	143.2	773	1.29	177	200	242	12.15
	845.2	25.8	50	43.7	773	1.29	177	200	242	13.08
	845.2	25.8	100	93.7	773	1.29	177	200	242	12.36
	845.2	25.8	150	143.7	773	1.29	177	200	242	11.70
	795.4	21.7	50	45.1	773	1.29	177	200	242	16.69
	795.4	21.7	100	95.1	773	1.29	177	200	242	15.92
	795.4	21.7	150	145.1	773	1.29	177	200	242	15.58
	747.5	25.9	50	44.5	773	1.29	177	200	242	18.75
	747.5	25.9	100	94.5	773	1.29	177	200	242	16.92
	747.5	25.9	150	144.5	773	1.29	177	200	242	15.94
	796.8	25.8	50	44.1	773	1.29	177	200	242	15.21
	796.8	25.8	100	94.1	773	1.29	177	200	242	13.77
	796.8	25.8	150	144.1	773	1.29	177	200	242	13.37

References

[1] Browne KR, Partridge IM, Greeves G. Fuel property effects on fuel/air mixing in an experimental diesel engine. SAE Paper 860233; 1986.

[2] Verhoeven D, Vanhemelryck JL, Baritaud T. Macroscopic and ignition characteristics of high-pressures sprays of single-component fuels. SAE Paper 981069; 1998.

[3] Canaan RE, Dec JE, Green RM, Daly DT. The influence of fuel volatility on the liquid-phase fuel penetration in a heavy-duty D.I. diesel engine. SAE Paper 980510; 1998.

[4] Higgins BS, Mueller CJ, Siebers D. Measurements of fuel effects on liquid-phase penetration in DI sprays, SAE Paper 1999-01-0519; 1999.

[5] Official Journal of the European Union, Directive 2003/30/EC of the European parliament and of the council of 8 May 2003 on the promotion of the use of biofuels or other renewable fuels for transport.

[6] Beatrice C, Guido C, Di Iorio S. Experimental analysis of alternative fuel impact on a new torque-controlled light-duty diesel engine for passenger cars. Fuel 2010;89:3278–86.

[7] Bermúdez V, García JM, Juliá E, Martínez S. Engine with optically accessible cylinder head: a research tool for injection and combustion processes. SAE Paper 2003-01-1110; 2003.

[8] Dec JE, Espey C. The effect of TDC temperature and density on the liquid-phase fuel penetration in a D.I. diesel engine. SAE Trans 1995;104(4):1400–14.

[9] Siebers DL. Liquid-phase fuel penetration in diesel sprays. SAE Trans 1998;107(3):1205–27.

[10] Payri R, Salvador FJ, Gimeno J, Zapata LD. Diesel nozzle geometry influence on spray liquid-phase fuel penetration in evaporative conditions. Fuel 2008;87(7):1165–76.

[11] Pastor JV, Pastor JM, Gimeno J, Nerva J-G. The effect of biodiesel fuel blend rate on the liquid-phase fuel penetration in diesel engine conditions, SAE Paper 2009-24-0051; 2009.

[12] Pastor JV, Payri R, Gimeno J, Nerva J-G. Experimental study on RME blends: liquid-phase fuel penetration, chemiluminescence, and soot luminosity in diesel-like conditions. Energy Fuels 2009;23(12):5899–915.

[13] Klein-Douwel RJH, Frijters PJM, Somers LMT, de Boer WA, Baert RSG. Macroscopic diesel fuel spray shadowgraphy using high speed digital imaging in a high pressure cell. Fuel 2007;86:1994–2007.

[14] Allocca L, Mancaruso E, Montanaro A, Sequino L, Vaglieco BM. Effects of mineral and biodiesel fuel compositions on spray evolution and mixture distribution. THIESEL Conference. Valencia, Spain; 2010.

[15] Siebers DL. Scaling liquid-phase fuel penetration in diesel sprays based on mixing – limited vaporization. SAE Trans 1999;108(3):703–728;.

[16] Baert RSG, Frijters PJM, Somers B, Luijten CCM, de Boer W. Design and operation of a high pressure, high temperature cell for HD diesel spray diagnostics: guidelines and results. SAE Paper 2009-01-0649; 2009.

[17] Pastor JV, Arrègle J, Palomares A. Diesel spray image segmentation with a likelihood ratio test. Appl Opt 2001;40:1–10;.

[18] Pastor JV, Arrègle J, García JM, Zapata LD. Segmentation of diesel spray images with loglikelihood ratio test algorithm for non-Gaussian distributions. Appl Opt 2007;46(6):888–99.

[19] Pastor JV, López JJ, García JM, Pastor JM. A 1D model for the description of mixing-controlled inert diesel sprays. Fuel 2008;87(13–14):2871–85.

[20] Musculus MPB, Kattke K. Entrainment waves in diesel jets. SAE Int J Eng 2009;2:1170–93.

[21] Desantes JM, Pastor JV, Payri R, Pastor JM. Experimental characterization of internal nozzle flow and diesel spray behavior. Part II. Evaporative conditions. Atomization Sprays 2005;15:517–43.

[22] Azimov U, Kim KS. Visualization of gas-to-liquid (GTL) fuel liquid length and soot formation in the constant volume combustion chamber. J Therm Sci Technol 2008;3:461–473;.

[23] Fisher BT, Knothe G, Mueller CJ. Liquid-phase penetration under unsteady in-cylinder conditions: soy- and cuphea-derived biodiesel fuels versus conventional diesel. Energy Fuels 2010;24:5163–5180;.

[24] Genzale CL, Pickett LM, Kook S. Liquid penetration of diesel and biodiesel sprays at late-cycle post-injection conditions. SAE Paper 2010-01-0610; 2010.

[25] Fisher BT, Mueller CJ. Liquid penetration length of heptamethylnonane and trimethylpentane under unsteady in-cylinder conditions. Fuel 2010;89:2673–96.